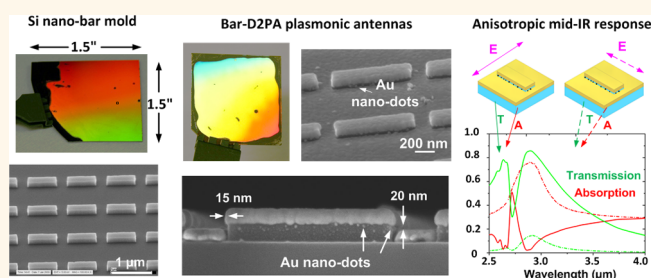


Plasmonic Bar-Coupled Dots-on-Pillar Cavity Antenna with Dual Resonances for Infrared Absorption and Sensing: Performance and Nanoimprint Fabrication

Chao Wang, Qi Zhang, Yu Song, and Stephen Y. Chou*

Department of Electrical Engineering, Princeton University, Princeton, New Jersey 08544, United States

ABSTRACT We report the structure, performance and large-area fabrication of a thin plasmonic infrared absorber, termed “bar-shaped disk-coupled dots-on-pillar antenna-array” (bar-D2PA). The bar-D2PAs, which are simple to fabricate, demonstrate the following, experimentally: (i) a different light-absorption resonance for each polarization with the resonance peak tunable by the bar-to-backplane gap and the bar size; (ii) for the geometry tested, the reflection is nearly constant at $\sim 10\%$, but the transmission and absorption highly depend upon the bar size and the gap between the bar and the backplane (*e.g.*, the absorption of 77% (30%), the transmission of 9% (62%), and the resonance peak at $3.12\ \mu\text{m}$ ($3.04\ \mu\text{m}$) for the polarization along 700 nm long (185 nm short) axis and a 20 nm gap); (iii) a smaller gap significantly enhances the normalized extraordinary transmission, and (iv) the extraordinary transmissions become larger as the polarized bar side is in deeper subwavelength. The bar-D2PAs were fabricated in large area using nanoimprint lithography, etching plus one metal deposition that forms all metal structures in one step with excellent self-alignment and self-assembly. The design and fabrication can be extended to broad plasmonic applications.



KEYWORDS: plasmonic nanostructures · nanobar absorber · disk-coupled dots-on-pillar cavity antenna array (D2PA) · nanoimprint lithography · infrared biochemical sensing · enhanced absorption · extraordinary transmission

Plasmonic absorbers,^{1,2} especially in near- and mid-infrared (IR), are of great interests due to their broad applications for biochemical sensing,^{3,4} imaging,⁵ energy conversion,⁶ medical diagnostics,⁷ *etc.* Plasmonic thin IR absorbers have been achieved in various nanostructures, including split-rings,^{8,9} coupled nanoparticles,^{10,11} metal–insulator–metal (MIM) structures,^{12–18} *etc.* Many of them have a single plasmonic resonant wavelength,^{12,13,17,18} and many have a low absorption (below 50%).^{8–11,19} Most of them require electron-beam lithography (EBL) that has limitations in small area, slow speed, and high cost by its serial writing nature,^{8–16} and others were fabricated by self-assembly based methods, such as nanosphere lithography and the like,^{18,19} that currently lack nanoscale fabrication precision.

Here we present a different structure of an efficient plasmonic IR absorber, termed “nanobar shaped disk-coupled dots-on-pillar antenna-array” (Bar-D2PA), which is an

advance of our previous circular D2PA.²⁰ The key advantages of bar-D2PA are the following: (a) one of the simplest high-performance light absorbers to fabricate, leading low-cost and wide applications; (b) multiple resonance peaks; (c) tunable absorption and transmission, with options of high (over 80%) absorption or high transmission; and (d) the high-field regions are accessible to the analytes to be sensed (rather than inaccessible in many current IR sensors).

RESULTS AND DISCUSSIONS

Bar-D2PA Structure and Operation Principle.

The bar-D2PA comprises a dielectric (or semiconductor) bar-shaped pillar array of subwavelength dimensions on a substrate with a metallic bar disk on top of each pillar, a perforated metallic backplane at the pillar foot, and metallic nanodots on the pillar sidewalls (Figure 1a,b). The metallic structures are arranged to have nanogaps between

* Address correspondence to chou@princeton.edu.

Received for review December 7, 2013 and accepted February 19, 2014.

Published online February 19, 2014
10.1021/nn406281u

© 2014 American Chemical Society

them. The entire complex metallic structures can be formed in one simple metal evaporation, as discussed below. The metallic disks and backplane form 3D cavities, which can trap the light inside with a high

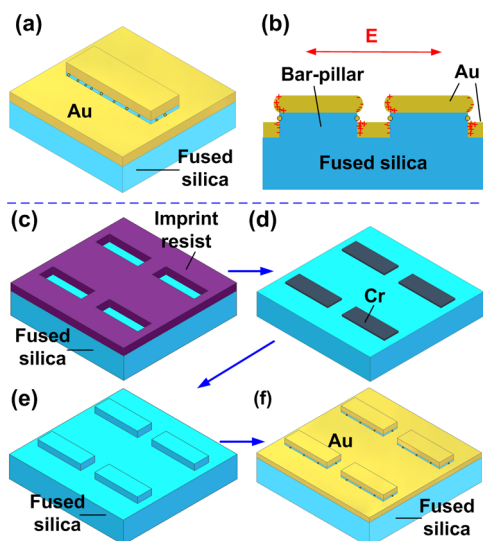


Figure 1. Schematics and NIL-fabrication process of plasmonic bar-D2PA antenna arrays. (a) Schematic plasmonic antenna, consisting of a fused silica nanobar pillar on fused silica substrate, a top Au nanobar disk, an Au nanohole backplane, and Au nanodots on pillar sidewalls. (b) Schematic charge coupling with applied electric field (red arrow). (c–f) Key fabrication steps: (c) NIL using a nanobar mold on fused silica, followed by oxygen RIE residual layer; (d) Cr nanobar liftoff; (e) RIE and Cr removal to form fused nanobars; and (f) Au evaporation to create self-aligned nanobar Au disks and Au backplane.

efficiency. The nanogaps between the metal components offer high local electric field.

Fabrication. The bar-D2PA is fabricated completely by nanoimprint lithography (NIL).²¹ Once a nanoimprint mold is made, the bar-D2PA fabrication is one of the simplest for nanoplasmonic structures, with the following key steps: (i) NIL and Cr liftoff to pattern a Cr nanobar array on a substrate (Figure 1c,d), (ii) reactive ion etching (RIE) to transfer the Cr array into the bar-shaped dielectric pillar array (Figure 1e), and (iii) after removing the Cr etching mask, metal (Au in this work) evaporation on the pillar array (Figure 1f).

The Au metal evaporation forms all the complex metallic structures (disks, backplane, and nanodots) of D2PA in one single step, and also self-aligns them to the correct positions: each bar metal disks are exactly aligned to each holes in the backplane with a fixed gap, and nanodots on the pillar sidewalls are aligned inside the nanogap.²⁰ The self-assembly of nanodots is from the instability of an Au ultrathin film on a nonwetting surface.

Nanofabrication of NIL Mold. We fabricated the NIL mold for bar-D2PA by a process termed “liftoff using a compositional-resist stack” (LUCS),²² which patterns rectangle nanobar into SiO₂ substrate by combining two cycles of orthogonal NIL with a grating mold, metal mask liftoff, and RIE (Figure 2). The grating mold in the second NIL cycle has a different line width and sometimes even a different period, making the final patterns of rectangle bar array with the same or different period in two orthogonal directions.

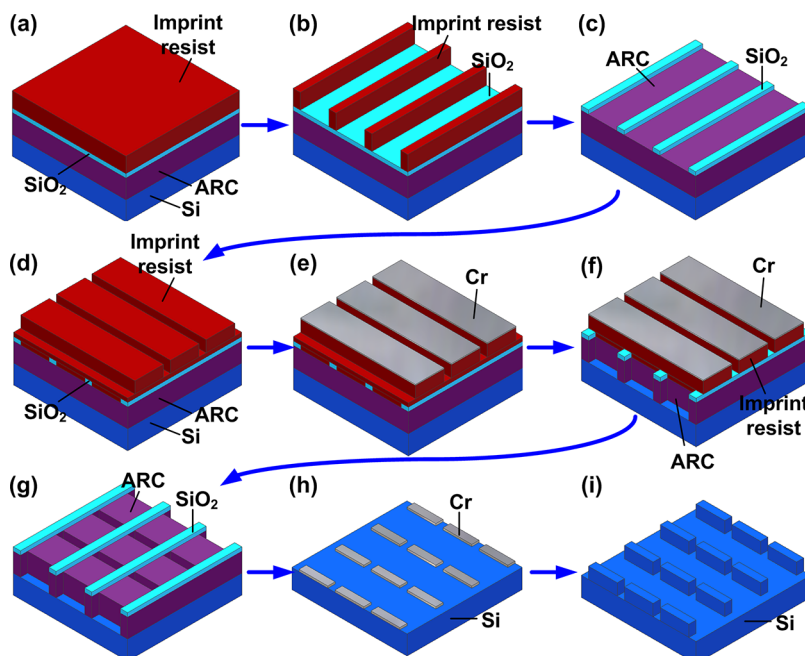


Figure 2. Fabrication schematics of a nanobar mold by NIL and LUCS: (a) Compositional resist stack (imprint resist/SiO₂/ARC) deposited on Si substrate; (b) first NIL and RIE top resist residual layer to define bar length; (c) RIE thin SiO₂ and stripping imprint resist by solvents; (d) deposition of second layer imprint resist and NIL to define bar width; (e) Cr shadow evaporation to cap resist gratings; (f) oxygen RIE into ARC layer; (g) stripping imprint resist; (h) Cr evaporation and liftoff; (i) Si RIE and Cr removal.

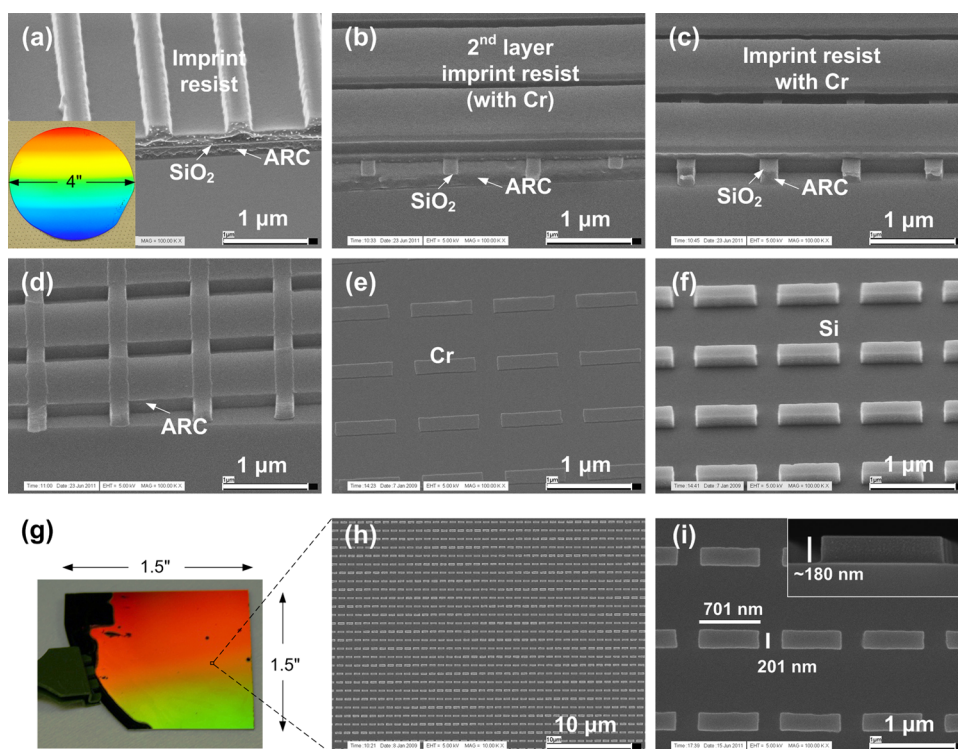


Figure 3. Fabrication process of a nanobar mold: (a–f) Side-view (tilted 45°) SEM images of (a) as-imprinted trilayer resist, with the optical image of master mold shown as insert; (b) imprinted second layer resist gratings (Cr coated) crossing SiO₂ gratings on top of ARC; (c) ARC nanobar openings after oxygen RIE; (d) ARC nanobar openings after stripping imprint resist with acetone; (e) Cr nanobars on Si after liftoff; and (f) Si nanobars after RIE and Cr etching. (g–i) Fabricated nanobar mold: (g) optical image, (h) large-area top-view SEM image, and (i) zoom-in top-view SEM image, with the cross-sectional image shown as insert.

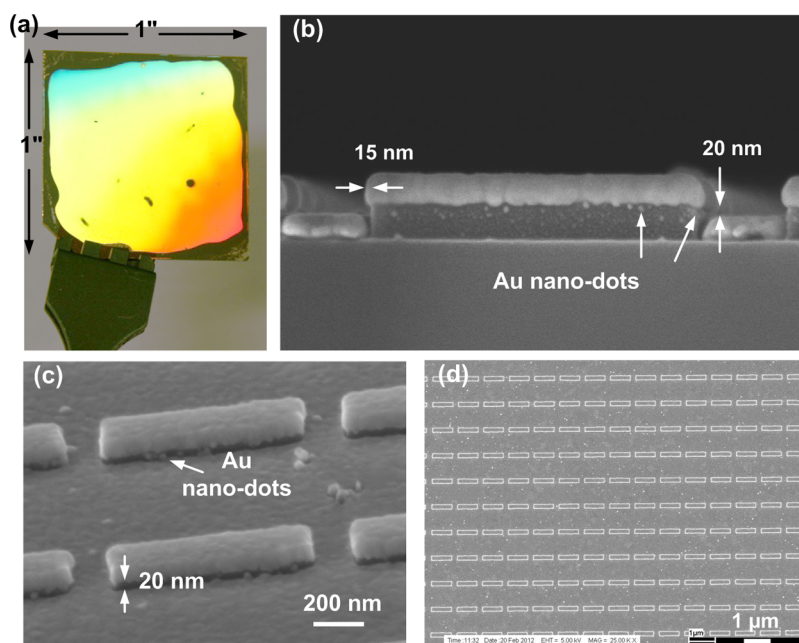


Figure 4. Optical and SEM images of fabricated plasmonic bar-D2PA absorbers: (a) Optical image of 1 in. bar-D2PA absorber chip; (b) cross-sectional view showing the vertical cavity, the overhang, and the self-assembled nanodots; (c) side-view (30° tilted); (d) large-scale top-view SEM image.

Briefly for the mold fabrication, the compositional resist stack (200 nm imprint resist, 15 nm SiO₂, and 150 nm cross-linked polymer ARC) was sequentially

imprinted using 4 in. grating molds (optical image Figure 3a), and further patterned by O₂ RIE to form bar-shaped nanoholes (scanning electron micrograph

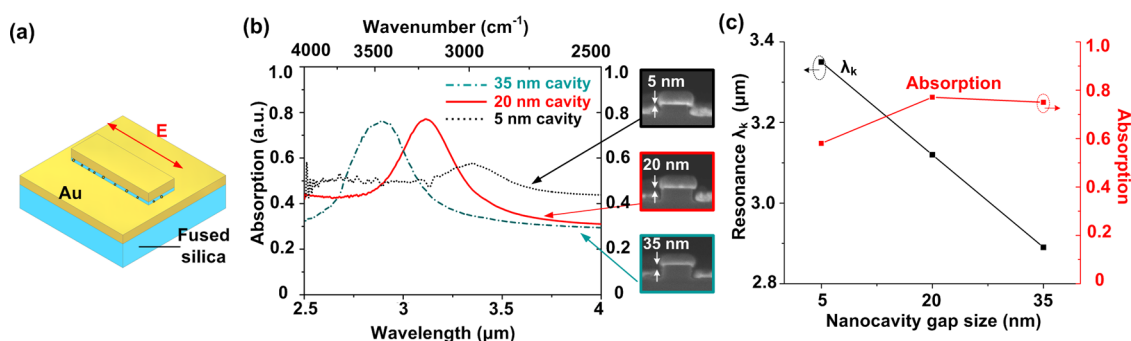


Figure 5. FTIR measured IR performance of plasmonic bar-D2PA with light polarization along the long-axis: (a) schematic of measurement; (b) FTIR-measured absorption spectra of three chips with 5 nm (black dot lines), 20 nm (red solid lines), and 35 nm (dark-cyan dash-dot lines) cavity gaps, with the cross-sectional SEM images shown as insert; (c) dependence of resonance wavelengths and absorption peaks on cavity gaps.

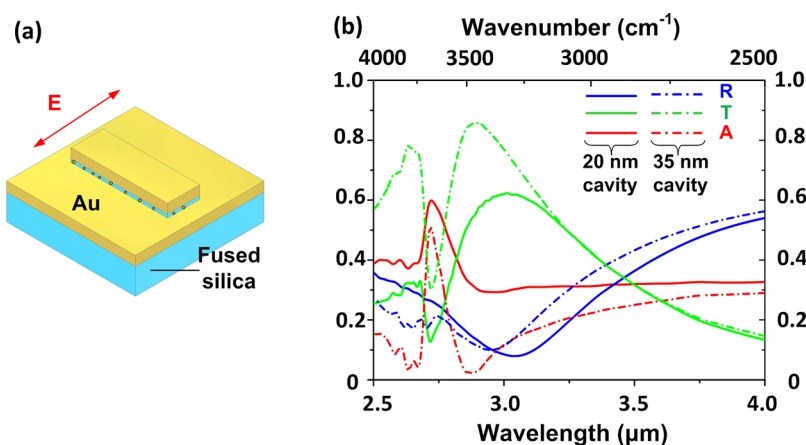


Figure 6. FTIR measured high transmission of bar-D2PA with light polarization along the short-axis: (a) schematic to show the electric field parallel to the short axis of bars; (b) FTIR-measured reflection (blue lines), transmission (green lines), and absorption (red lines) spectra for absorbers with 20 nm (solid lines) and 35 nm (dash-dot lines) cavities.

(SEM) Figure 3a–d). Then Cr liftoff and RIE created the nanobars into the Si mold substrate (Figure 3 e-i). Finally, the etching mask materials were removed from the Si mold substrate by oxygen plasma, CR-7 (Cyantek) and RCA-1 solution ($\text{NH}_4\text{OH}:\text{H}_2\text{O}_2:\text{DI water} = 1:1:5$, 80 °C, 20 min), and then the mold was diced and coated with an antisticking mold release agent (Nanonex NXT-110). The NIL and LUCS based method allows uniform patterning and flexible design of various nanobar geometries and dimensions (Supporting Information Figure S1), which are all desirable for optimizing the IR plasmonic sensors.²³

Bar-D2PA Absorber Fabrication. Using the fabricated 950 nm period bar-mold, we patterned nanobar pillars (700 nm long, 185 nm wide, and 70 nm high) on 1 in. square fused silica chips by NIL, Cr liftoff, and RIE. The silica chips were thoroughly cleaned by oxygen plasma, CR-7 and RCA-1, and then deposited with 50 nm thick Au to form bar-D2PA antennas (Figure 4a,b) with a 20 nm disk-to-backplane gap (Figure 4c). The Au deposition (0.5 Å/s) created a ~ 15 nm Au overhang on silica pillar perimeters and also Au nanodots (5–10 nm diameter) on the sidewall (Figure 4c,d). The bar-D2PA sensors with nominal gaps (the distance

between the metal disk and backplane) of 5 and 35 nm were formed using nominal pillar heights of 55 and 85 nm and an Au film thickness of 50 nm.

Performance of Bar-D2PA IR Absorbers. *Polarization along Bar Long-Axis.* The transmission and reflection spectra (T, R) of the bar-D2PAs were measured in air using Fourier transform infrared spectroscopy (FTIR) (schematic Figure 5a, experimental data Supporting Information Figure S2). The absorption spectra were obtained by $A = 1 - T - R$ (Figure 5b). For light polarized along bar long-axis, the measured optical spectra of bar-D2PA (700/185 nm in bar length/width) with a 20 nm gap show a resonance peak, λ_k , at $3.12 \mu\text{m}$ (3210 cm^{-1}), a narrow line width (full-width-half-maximum (fwhm)) of $0.34 \mu\text{m}$ (a high Q -factor $\lambda_k/\text{fwhm} = 9.2$), $R = 13.8\%$, $T = 9\%$, and $A = 77.2\%$ at resonance. For a 35 nm gap, which means a weaker coupling between the metal bar and the backplane than the 20 nm gap, the bar-D2PA's resonance wavelength was blue-shifted significantly to $2.89 \mu\text{m}$ (3460 cm^{-1}), shifting 230 nm (15.3 nm shift per each nanometer change in the gap), and the peak absorption was nearly unchanged at 76% (Figure 5b,c). For a nominal 5 nm gap, λ_k was indeed red-shifted by 230 nm to $3.35 \mu\text{m}$ compared to a 20 nm gap, but the peak absorption was

reduced to 58% (Figure 5b,c). The absorption reduction could be caused by the electrical shorting between the disk and the backplane by Au nanodots in the gap.

The absorption of bar-D2PA (>76% in a nonshorting cavity) is 2–8 times higher than a single layer of Au single-bars (10% at $3.6 \mu\text{m}$)³ or bar-arrays on an insulator substrate ($\sim 30\%$ at $1.7 \mu\text{m}$).⁴ The markedly increased absorption of the bar-D2PA absorbers is attributed to the efficient light collection and trapping by the cavity antennas of the bar-D2PA.²⁰ Compared to conventional metal–insulator–metal (MIM) plasmonic structures,^{12–14,17,18} the bar-D2PA has the highest electric field region open to deposited molecules for sensitive detection (from Zhang and Chou, unpublished data), while the MIM has the highest field region inaccessible.

Polarization along Bar Short-Axis. For incident light polarized along bar short-axis (Figure 6), λ_k is 3.04 and $2.95 \mu\text{m}$ and fwhm is 0.94 and $0.92 \mu\text{m}$ for the 20 and 35 nm gaps, respectively (Figure 6). Again, a smaller gap red-shifts the resonant peak, but the shift is smaller

than in the long-axis case. The shift of 90 nm corresponds to 6 nm in wavelength per nanometer change in gap. In addition to the gap-dependent resonance peaks for polarizations in both bar directions, a gap-independent absorption of $\sim 60\%$ at $2.72 \mu\text{m}$ ($\sim 3675 \text{ cm}^{-1}$) was observed, which is attributed to the absorption of fused silica substrate.²⁴

Interestingly, for short-axis polarization, the peak transmission was very high, *i.e.*, 61.9% and 86.3% for 20 and 35 nm gap, respectively, although the bar holes are completely blocked; namely, there is no geometric straight light path between two sides of the bar-D2PA. Furthermore, even considering the areas uncovered by Au, which are on the pillar sidewall and in the shadow of the metal bar overhang (hence, no straight path for being accessed by incoming light), the extraordinary normalized-to-area transmission is 1590% and 1250% for 20 and 35 nm gap, respectively (Table 1). Such an extraordinary light transmission over the blocked holes in a thin metal film has been observed previously in round D2PA structures and is attributed to the antenna nature of D2PA.²⁵ Compared with the transmission for the light polarized in the long axis (700 nm), the transmission in the short axis (185 nm) is about 6–7 times higher for the given nanogaps.

The experimentally determined mid-IR optical properties of bar-D2PA are summarized in Table 1. Interestingly, the reflection stayed relatively constant at $\sim 10\%$, but the transmission and absorption are highly polarization-dependent: high absorption (low transmission) with long-axis polarization while high transmission (low absorption) with short-axis polarization.

TABLE 1. Experimentally Determined Optical Response of Bar-D2PA with a Nonshorting Cavity

polarization	cavity gap			normalized T	λ_k (μm)	fwhm (μm)	Q-factor
	(nm)	T	R				
long axis (700 nm)	20	9.0%	13.8%	77.2%	230%	3.12	0.34
	35	10.0%	14.0%	76.0%	145%	2.89	0.40
short axis (185 nm)	20	61.9%	7.9%	30.2%	1590%	3.04	0.94
	35	86.3%	12.5%	1.2%	1250%	2.89	0.92

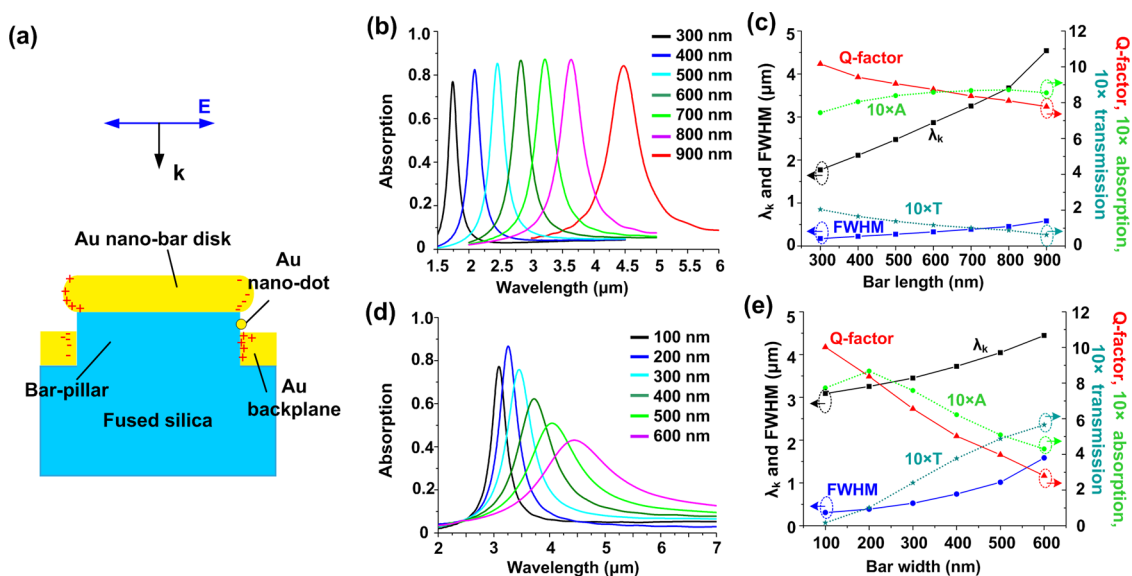


Figure 7. Calculation of resonance tuning of bar-D2PA by bar lengths/widths using FDTD simulation. (a) Model of a bar-D2PA unit cell for the simulation (20 nm nanogap, with a single 10 nm nanodot in cavity). (b and c) Simulated absorption as a function of the bar lengths (bar width fixed as 185 nm): (b) simulated absorption spectra, and (c) dependence of resonance wavelengths λ_k , fwhm's, Q-factors (λ_k/fwhm), absorption peaks, and transmission peaks on nanobar length. (d and e) Tuning of IR performance by changing bar widths (bar length fixed as 700 nm): (d) calculated absorption spectra, and (e) dependence of λ_k , fwhm's, Q-factors, absorption peaks, and transmission peaks on nanobar width. In the simulation, the polarization is always assumed along the bar long-axis.

Such polarization-sensitive spectra indicate plasmonic bar-D2PA can behave as either a bar-antenna or a nanohole, which can be useful in subwavelength lithography,²⁶ nano-optics (filters, polarizers, *etc.*) and imaging,²⁷ biomolecular sensing,²⁸ and many others.

Simulation. The bar-D2PA properties were further studied using a finite-difference time-domain (FDTD) tool (Lumerical Solutions, Inc.), and a 3D model (Figure 7a) with experimental structural and material parameters and established optical constants.^{29,30} Lateral periodic boundaries, vertical perfectly matched layer (PML) and normal incidence plane-wave polarized along bar long-axis were used. One Au nanodot of 10 nm diameter was assumed on the pillar sidewall.

The simulation (Figure 7b,c) also shows the effects of bar length (300–900 nm) on bar-D2PA's absorption and transmission with fixed 185 nm bar width and 20 nm gap: (a) the absorption is high (>75%) from a low transmission (<20%); (b) λ_k linearly increases from 1.78 to 4.54 μm at a slope of ~ 4.6 ; (c) fwhm increases from 180 to 580 nm at a slope of 0.6; and (d) the Q -factor (λ_k/fwhm) slightly reduces from 10.2 to 7.8 but is still quite large. When increasing bar-width from 100 to 600 nm with a fixed length 700 nm (Figure 7d,e), λ_k can be tuned from 3.09 to 4.45 μm at a slope of ~ 2.7 . However, larger bar-width leads to decreased absorption (*e.g.*, only 43% at 600 nm width) due to enhanced transmission (57%), a wider resonance ($\sim 1.6 \mu\text{m}$ fwhm), and significantly dropped Q -factor (from 10 to 2.8, >70% reduction) (Figure 7d,e). Clearly, a bar-D2PA with a narrow bar-width (*e.g.*, < 200 nm) is advantageous for sensitive and selective biochemical detection,^{23,31–34} which

requires widely tunable, narrow, and high-absorption resonance. The simulation is also in good agreement with our measured results (*e.g.*, $A, T, R, \lambda_k = 87.3\%, 7.9\%, 4.8\%, 3.20 \mu\text{m}$ in simulation and 77.2%, 9.0%, 13.8%, 3.12 μm in experiment for 20 nm gap). The high absorption can be attributed to D2PA structure itself, which has demonstrated >95% absorption with a round pillar.³⁵

CONCLUSIONS

We demonstrate a plasmonic bar-D2PA IR absorber with an ultrathin active layer (~ 120 nm) and its large-area fabrication completely based on NIL without any e-beam writing. The bar-D2PA structure shows unique mid-IR light response with polarization-dependent plasmonic resonances. With long-axis polarization, we demonstrate a high-IR absorption (77%), a large resonance tuning by vertical disk-backplane gap (230 nm in wavelength from 15 nm gap change), and a flexible and long-range (1.8–4.5 μm) resonance tuning by nanobar length (300–900 nm). On the other hand, with short-axis polarization, an extraordinary normalized-to-area transmission of 1590% (20 nm cavity) is realized. These demonstrated plasmonic properties in flexible resonance tuning, polarization-sensitive high absorption/transmission, *etc.* are very useful to various applications, such as molecular detection,^{20,31} imaging, cancer therapy,³⁶ and so on. The NIL and LUCS based fabrication method make our approach ideal for large-scale production, and can be extended to other complex structures such as fish-net structures and split-rings, among others.

METHODS AND MATERIALS

Fabrication of Nanobar Mold. Nanoimprint was carried out using Nanonex NX-2000 imprinter at 130 °C and 200 psi for 5 min. The imprint resist (NXR-1025, Nanonex Corp.) was 200 nm thick by spin-coating, and the underlayer polymer ARC (XHRiC-16, Brewer Science, Inc.) was baked 30 min at 180 °C prior to use with a thickness of ~ 150 nm after baking. The Cr cap on resist grating was deposited by a bidirectional shadow evaporation (2 nm each side, $\sim 70^\circ$ from wafer normal) to cover only the resist grating top but not in the trench. To liftoff Cr nanobar mask, the Cr-deposited Si wafer was rinsed with solvents (acetone and 2-propanol), soaked in RCA-1 for 15 min, rinsed with DI wafer, and N_2 dried. After Si nanobar etching, the wafer was cleaned with oxygen plasma (15 min), soaked in CR-7 (Cyantek) to strip Cr, cleaned in RCA-1 solution for 20 min, and coated with an antisticking mold release agent (Nanonex NXT-110).

Fabrication of Bar-D2PA. The imprint procedure was the same as above, and the residual layer was etched by oxygen plasma prior to Cr mask evaporation. The evaporated Cr nanobars were lifted off by acetone spray-gun rinsing. The fused silica nanobar pillars were etched by CF_4/H_2 RIE (33/7 sccm, 50 mTorr, 300 W). The fused silica chips were cleaned by CR-7 Cr etch (Cyantek), oxygen plasma, and 15 min RCA-1 before Au deposition. The Au layer was deposited at a rate of 0.5 $\text{\AA}/\text{s}$ (Temescal BJD-1800, chamber temperature ~ 60 °C after evaporation) and normal to fused silica chips.

Conflict of Interest: The authors declare no competing financial interest.

Acknowledgment. We greatly appreciate Prof. Claire F. Gmachl for valuable help and discussions on mid-IR measurement, and thank Dr. Patrick Murphy and Dr. Wendi Li for making the master grating mold. We also thank Defense Advanced Research Program Agency (DARPA) and National Science Foundation (NSF) for funding and support.

Supporting Information Available: Additional nanobar fabrication and IR spectra data (Figures S1–S2). This material is available free of charge via the Internet at <http://pubs.acs.org>.

REFERENCES AND NOTES

- Anker, J. N.; Hall, W. P.; Lyandres, O.; Shah, N. C.; Zhao, J.; Van Duyne, R. P. Biosensing with Plasmonic Nanosensors. *Nat. Mater.* **2008**, *7*, 442–453.
- Mayer, K. M.; Hafner, J. H. Localized Surface Plasmon Resonance Sensors. *Chem. Rev.* **2011**, *111*, 3828–3857.
- Neubrech, F.; Pucci, A.; Cornelius, T. W.; Karim, S.; Garcia-Etxarri, A.; Aizpurua, J. Resonant Plasmonic and Vibrational Coupling in a Tailored Nanoantenna for Infrared Detection. *Phys. Rev. Lett.* **2008**, *101*, 157403.
- Adato, R.; Yanik, A. A.; Amsden, J. J.; Kaplan, D. L.; Omenetto, F. G.; Hong, M. K.; Erramilli, S.; Altug, H. Ultra-Sensitive Vibrational Spectroscopy of Protein Monolayers with Plasmonic Nanoantenna Arrays. *Proc. Natl. Acad. Sci. U. S. A.* **2009**, *106*, 19227–19232.
- Kawata, S.; Inouye, Y.; Verma, P. Plasmonics for Near-Field Nanoimaging and Superlensing. *Nat. Photonics* **2009**, *3*, 388–394.

6. Knight, M. W.; Sobhani, H.; Nordlander, P.; Halas, N. J. Photodetection with Active Optical Antennas. *Science* **2011**, *332*, 702–704.
7. Huang, X.; El-Sayed, I. H.; Qian, W.; El-Sayed, M. A. Cancer Cell Imaging and Photothermal Therapy in the Near-Infrared Region by Using Gold Nanorods. *J. Am. Chem. Soc.* **2006**, *128*, 2115–2120.
8. Cubukcu, E.; Zhang, S.; Park, Y. S.; Bartal, G.; Zhang, X. Split Ring Resonator Sensors for Infrared Detection of Single Molecular Monolayers. *Appl. Phys. Lett.* **2009**, *95*, 043113.
9. Pryce, I. M.; Kelaita, Y. A.; Aydin, K.; Atwater, H. A. Compliant Metamaterials for Resonantly Enhanced Infrared Absorption Spectroscopy and Refractive Index Sensing. *ACS Nano* **2011**, *5*, 8167–8174.
10. Atay, T.; Song, J. H.; Nurmikko, A. V. Strongly Interacting Plasmon Nanoparticle Pairs: From Dipole-Dipole Interaction to Conductively Coupled Regime. *Nano Lett.* **2004**, *4*, 1627–1631.
11. Dregely, D.; Hentschel, M.; Giessen, H. Excitation and Tuning of Higher-Order Fano Resonances in Plasmonic Oligomer Clusters. *ACS Nano* **2011**, *5*, 8202–8211.
12. Liu, N.; Mesch, M.; Weiss, T.; Hentschel, M.; Giessen, H. Infrared Perfect Absorber and Its Application as Plasmonic Sensor. *Nano Lett.* **2010**, *10*, 2342–2348.
13. Liu, X.; Starr, T.; Starr, A. F.; Padilla, W. J. Infrared Spatial and Frequency Selective Metamaterial with Near-Unity Absorbance. *Phys. Rev. Lett.* **2010**, *104*, 207403.
14. Ameling, R.; Langguth, L.; Hentschel, M.; Mesch, M.; Braun, P. V.; Giessen, H. Cavity-Enhanced Localized Plasmon Resonance Sensing. *Appl. Phys. Lett.* **2010**, *97*, 253116.
15. Jiang, Z. H.; Yun, S.; Toor, F.; Werner, D. H.; Mayer, T. S. Conformal Dual-Band Near-Perfectly Absorbing Mid-Infrared Metamaterial Coating. *ACS Nano* **2011**, *5*, 4641–4647.
16. Chen, K.; Adato, R.; Altug, H. Dual-Band Perfect Absorber for Multispectral Plasmon-Enhanced Infrared Spectroscopy. *ACS Nano* **2012**, *6*, 7998–8006.
17. Cattoni, A.; Ghenuche, P.; Haghiri-Gosnet, A. M.; Decanini, D.; Chen, J.; Pelouard, J. L.; Collin, S. $\lambda(3)/1000$ Plasmonic Nanocavities for Biosensing Fabricated by Soft UV Nanoimprint Lithography. *Nano Lett.* **2011**, *11*, 3557–3563.
18. Ye, J.; Shioi, M.; Lodewijks, K.; Lagae, L.; Kawamura, T.; Dorpe, P. V. Tuning Plasmonic Interaction between Gold Nanorings and a Gold Film for Surface Enhanced Raman Scattering. *Appl. Phys. Lett.* **2010**, *97*, 163106.
19. Bukasov, R.; Shumaker-Parry, J. S. Highly Tunable Infrared Extinction Properties of Gold Nanocrescents. *Nano Lett.* **2007**, *7*, 1113–1118.
20. Li, W. D.; Ding, F.; Hu, J.; Chou, S. Y. Three-Dimensional Cavity Nanoantenna Coupled Plasmonic Nanodots for Ultrahigh and Uniform Surface-Enhanced Raman Scattering over Large Area. *Opt. Express* **2011**, *19*, 3925–3936.
21. Chou, S. Y.; Krauss, P. R.; Renstrom, P. J. Nanoimprint Lithography. *J. Vac. Sci. Technol., B* **1996**, *14*, 4129–4133.
22. Wang, C.; Chou, S. Y. Integration of Metallic Nanostructures in Fluidic Channels for Fluorescence and Raman Enhancement by Nanoimprint Lithography and Lift-Off on Compositional Resist Stack. *Microelectron. Eng.* **2012**, *98*, 693–697.
23. Huang, X. H.; Neretina, S.; El-Sayed, M. A. Gold Nanorods: From Synthesis and Properties to Biological and Biomedical Applications. *Adv. Mater.* **2009**, *21*, 4880–4910.
24. Heilweil, E. J.; Casassa, M. P.; Cavanagh, R. R.; Stephenson, J. C. Temperature Dependence of the Vibrational Population Lifetime of $\text{OH}(\nu = 1)$ in Fused Silica. *Chem. Phys. Lett.* **1985**, *117*, 185–190.
25. Li, W.-D.; Hu, J.; Chou, S. Y. Extraordinary Light Transmission through Opaque Thin Metal Film with Subwavelength Holes Blocked by Metal Disks. *Opt. Express* **2011**, *19*, 21098–21108.
26. Srituravanich, W.; Fang, N.; Sun, C.; Luo, Q.; Zhang, X. Plasmonic Nanolithography. *Nano Lett.* **2004**, *4*, 1085–1088.
27. Laux, E.; Genet, C.; Skauli, T.; Ebbesen, T. W. Plasmonic Photon Sorters for Spectral and Polarimetric Imaging. *Nat. Photonics* **2008**, *2*, 161–164.
28. Brolo, A. G.; Gordon, R.; Leathem, B.; Kavanagh, K. L. Surface Plasmon Sensor Based on the Enhanced Light Transmission through Arrays of Nanoholes in Gold Films. *Langmuir* **2004**, *20*, 4813–4815.
29. Ordal, M. A.; Long, L. L.; Bell, R. J.; Bell, S. E.; Bell, R. R.; Alexander, R. W.; Ward, C. A. Optical-Properties of the Metals Al, Co, Cu, Au, Fe, Pb, Ni, Pd, Pt, Ag, Ti, and W in the Infrared and Far Infrared. *Appl. Opt.* **1983**, *22*, 1099–1119.
30. Malitson, I. H. Interspecimen Comparison of the Refractive Index of Fused Silica. *J. Opt. Soc. Am.* **1965**, *55*, 1205–1208.
31. Kabashin, A. V.; Evans, P.; Pastkovsky, S.; Hendren, W.; Wurtz, G. A.; Atkinson, R.; Pollard, R.; Podolskiy, V. A.; Zayats, A. V. Plasmonic Nanorod Metamaterials for Biosensing. *Nat. Mater.* **2009**, *8*, 867–871.
32. Link, S.; El-Sayed, M. A. Spectral Properties and Relaxation Dynamics of Surface Plasmon Electronic Oscillations in Gold and Silver Nanodots and Nanorods. *J. Phys. Chem. B* **1999**, *103*, 8410–8426.
33. Sonnichsen, C.; Franzl, T.; Wilk, T.; von Plessen, G.; Feldmann, J.; Wilson, O.; Mulvaney, P. Drastic Reduction of Plasmon Damping in Gold Nanorods. *Phys. Rev. Lett.* **2002**, *88*, 077402.
34. Becker, J.; Trugler, A.; Jakab, A.; Hohenester, U.; Sonnichsen, C. The Optimal Aspect Ratio of Gold Nanorods for Plasmonic Bio-Sensing. *Plasmonics* **2010**, *5*, 161–167.
35. Zhou, L.; Ding, F.; Chen, H.; Ding, W.; Zhang, W.; Chou, S. Y. Enhancement of Immunoassay's Fluorescence and Detection Sensitivity Using Three-Dimensional Plasmonic Nano-Antenna-Dots Array. *Anal. Chem.* **2012**, *84*, 4489–4495.
36. Huang, X. H.; Jain, P. K.; El-Sayed, I. H.; El-Sayed, M. A. Gold Nanoparticles: Interesting Optical Properties and Recent Applications in Cancer Diagnostic and Therapy. *Nanomedicine* **2007**, *2*, 681–693.